The Astrophysical Journal, 727:25 (12pp), 2011 January 20 doi:10.1088/0004-637X/727/1/25

COMPARING SPATIAL DISTRIBUTIONS OF SOLAR PROMINENCE MASS DERIVED FROM CORONAL ABSORPTION

Holly Gilbert[1], Gary Kilper[1], David Alexander[2], and Therese Kucera[1]
[1] NASA Goddard Space Flight Center, Code 670, Greenbelt, MD 20771, USA; holly.r.gilbert@nasa.gov
[2] Department of Physics and Astronomy, Rice University, Houston, TX 77005, USA
Received 2010 July 12; accepted 2010 November 12; published 2010 December 28

ABSTRACT

In a previous study, Gilbert et al. derived the column density and total mass of solar prominences using a new technique, which measures how much coronal radiation in the Fe XII (195 Å) spectral band is absorbed by prominence material, while considering the effects of both foreground and background radiation. In the present work, we apply this method to a sample of prominence observations in three different wavelength regimes: one in which only H^0 is ionized (504 Å $< \lambda <$ 911 Å), a second where both H^0 and He^0 are ionized (228 Å $< \lambda <$ 504 Å), and finally at wavelengths where H^0, He^0, and He^+ are all ionized ($\lambda <$ 228 Å). This approach, first suggested by Kucera et al., permits the separation of the contributions of neutral hydrogen and helium to the total column density in prominences. Additionally, an enhancement of the technique allowed the calculation of the two-dimensional (2D) spatial distribution of the column density from the continuum absorption in each extreme-ultraviolet observation. We find the total prominence mass is consistently lower in the 625 Å observations compared to lines in the other wavelength regimes. There is a significant difference in total mass between the 625 Å and 195 Å lines, indicating the much higher opacity at 625 Å is causing a saturation of the continuum absorption and thus, a potentially large underestimation of mass.

Key words: Sun: abundances – Sun: chromosphere – Sun: filaments, prominences

Online-only material: color figures

1. INTRODUCTION

Prominences, relatively cool objects suspended in the hotter corona, are composed primarily of helium and hydrogen, but little is known about their exact composition. Generally, it is assumed that they are composed of 10% helium and 90% hydrogen by number, which is based on the typical cosmic abundance. Although the composition has not yet been directly measured, observations of prominences in the extreme-ultraviolet (EUV) offer a relatively straightforward approach to inferring prominence mass (Gilbert et al. 2005), a task that in Hα observations is nearly intractable due to the complicated radiative transfer for Hα emission. Prominence absorption features in coronal EUV lines are caused by photoionization of H^0, He^0, and/or He^+ in the prominence plasma, which depends on the wavelength (Kucera et al. 1998). The H^0, He^0, and He^+ continua have upper bounds of 911 Å, 504 Å, and 228 Å, respectively (Figure 1).

In the EUV, both transition region and coronal lines have been used to study prominences (Kucera et al. 1998; Schmieder et al. 1998, 2003, 2004; Golub et al. 1999; Penn 2000; Mein et al. 2001; Del Zanna et al. 2004). Del Zanna et al. (2004) found a neutral He/H ratio of 0.1–0.2 by using several transition region lines and considering two prominence models: one in which the filamentary structure and inter-thread gas have the same temperature with a temperature transition region surrounding the whole prominence body, and the other in which each thread of the filamentary structure is surrounded by a tube-like transition region. Other studies measured the amount of absorption in coronal EUV observations due to prominence material to deduce prominence densities and prominence column densities (Kucera et al. 1998; Golub et al. 1999; Penn 2000; Mein et al. 2001). Motivating the present study, Kucera et al. suggested looking at prominence absorption in several different coronal lines spanning each ionization wavelength regime (see Figure 1) to determine the absolute abundances of neutral helium and hydrogen in prominences.

By observing how much coronal radiation is absorbed by a prominence low in the solar atmosphere in the EUV, it is possible to infer its mean column density and thence obtain a total prominence mass. Gilbert et al. (2005, 2006) previously applied such a technique to *Solar and Heliospheric Observatory* (*SOHO*) EIT 195 Å observations to infer prominence mass. This technique involves calculating prominence column mass density along the line of sight, and subsequently integrating this column mass density over the prominence area to find the total mass. It also allows the effects of both foreground and background radiation to be considered.

In the present work, we extend the use of this mass-inference technique to a sample of prominences observed in at least two coronal lines. This approach, in theory, allows a direct calculation of prominence mass and helium abundance, and how these properties vary spatially and temporally. Obtaining an He/H abundance ratio relies on the theoretical expectation that the amount of absorption at each EUV wavelength is well characterized. However, in this work we show that due to a saturation of the continuum absorption in the 625 Å and 368 Å lines (which have much higher opacity compared to 195 Å; Heinzel et al. 2001, 2003, 2008) the uncertainties in obtaining the relative abundances are too high to give meaningful estimates. This is an important finding because of its impact on future studies in this area.

Section 2 of this paper contains a description of the observations, and Section 3 summarizes the method used to infer mass along with the criteria imposed in choosing prominences appropriate for this study. Section 3 also contains a discussion of the problems due to limitations of the available data and the implications for determining relative abundances. We present our results in Section 4, and the last section contains a

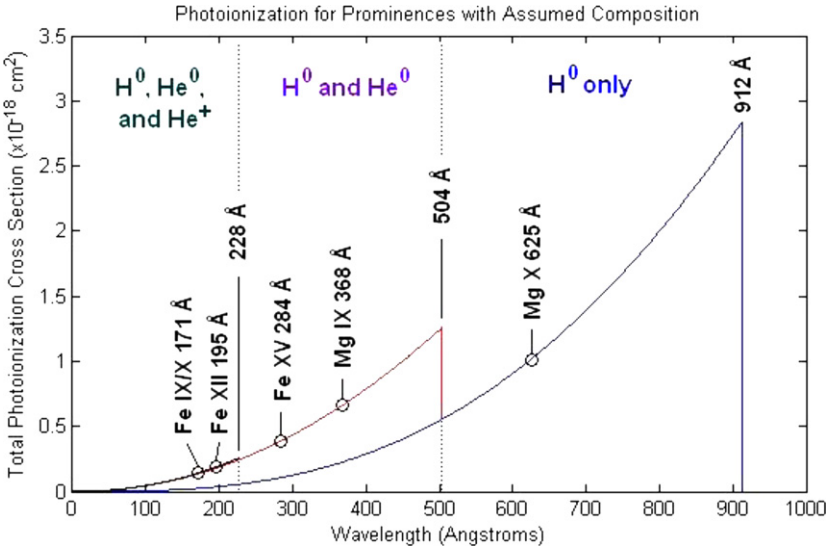

Figure 1. Average photoionization cross section per atom/ion in a prominence with an assumed composition (45% H^0, 45% H^+, 9% He^0, and 1% He^+). In this plot, the contributions to the total photoionization cross section are separated by the absorbing species: those due to H^0 (below the blue line), He^0 (between the red and blue lines), and He^+ (between the black and red lines) start at 912 Å, 504 Å, and 228 Å, respectively (Kilper 2009; Keady & Kilcrease 2000).

(A color version of this figure is available in the online journal.)

Table 1
Summary of Observations

Instrument	Wavelength (Å)	Spectral Bandpass (Å)	Pixel Size (arcsec)	Field of View (arcsec)	Cadence
CDS NIS1	368	0.08	4.06 × 1.68	120 × 240	68 minutes
CDS NIS2	625	0.14	4.06 × 1.68	120 × 240	68 minutes
CDS[a]	368/625	0.08/0.14	2.03 × 1.68	244 × 240	105 minutes
CDS[b]	368/625	0.08/0.14	4.06 × 3.36	244 × 240	44 minutes
EIT	195	13	5.25	Full disk	12 minutes
EIT	171	12	2.63	Full disk	6 hr
TRACE	171	6.4	0.5	384 × 384	60 s

Notes.
[a] Program for the CDS observations of a prominence on 1996 July 31.
[b] Program for the 18 successive CDS observations on 2005 May 18.

discussion summarizing the importance of the results found in this work. The appendices provide a detailed derivation of how to obtain prominence mass and helium abundance (Appendix A) and include the data for all prominences studied (Appendix B).

2. DATA

Table 1 summarizes the data used in this paper. The primary observations used in the present study are from the Coronal Diagnostic Spectrometer (CDS)/Normal Incidence Spectrometer (NIS) on board *SOHO*, a complete description of which can be found in Harrison et al. (1995). We selected two lines in which prominences are observed in absorption in the CDS data: Mg IX (λ368) and Mg X (λ625). Most of the observations we analyzed were taken via Joint Observing Program 63 (JOP 63; led by T. Kucera and V. Andretta), which used the 4″ × 240″ slit, integrated over 120 s for 30 steps to create a rastered image in 64 minutes with a 120 × 240 arcsec field of view (FOV). The observations for 1996 July 31 and 2005 May 18 used different observing sequences, which are outlined in Table 1, and have a larger 244 × 240 arcsec FOV. An important selection effect is that these prominences had to be small enough azimuthally to fit within the FOV, in order to have points on both sides of the prominence material from which the interpolation of the background corona is performed. We also used observations taken at wavelengths Fe XII (λ195) and Fe IX/X (λ171) from the Extreme Ultraviolet Imaging Telescope (EIT; Delaboudinière et al. 1995) on board *SOHO* and Fe IX/X (λ171) from the *Transition Region And Coronal Explorer* (*TRACE*) telescope (Handy et al. 1999). EIT images the solar transition region and inner corona in four bandpasses in the EUV, having a temporal cadence of three to five images a day (except for λ195 in which an image is taken every 12–20 minutes) *TRACE* observes a fraction of the full solar disk at high spatial (0.5 arcsec pixel^{-1}) and temporal (60 s) resolution.

3. APPROACH

Our first criterion for selecting prominences is the stipulation that they are visible in the 625 Å line and at least one other line used in the study (λ368, λ195, or λ171) and do not appear to be totally opaque to the background coronal radiation, with a preference for those "straddling" the limb so that the spatial-interpolative method of Gilbert et al. (2005) can easily be applied. The Mg IX (368 Å) and Mg X (625 Å) lines were chosen because prominences are easily detected in absorption in those lines, and to benefit from using data produced by the same instrument (CDS). The Fe IX/X (171 Å) and Fe XII (195 Å) bands are used as an augmentation and are crucial when Mg IX is not available. Although not directly visible, we require an indication

that background radiation exists to penetrate the absorbing prominence (determined by looking at the surrounding coronal environment). One last condition is that at least part of the prominence must appear uniform to minimize the effects of variations of the prominence column density (see Gilbert et al. 2005). We analyzed nine non-erupting prominences that fit these criteria, which were observed by CDS and the other instruments during various years over the time period of 1996–2007.

Our initial approach involves using the combination of two spectral lines to directly calculate total mass and helium abundance. We outline how that can be accomplished in a detailed derivation in Appendix A. Below we describe the basic approach followed by a discussion of why and how we adjusted the more detailed approach (Appendix A) to include the effect of saturation of the continuum absorption in the EUV at 625 Å and 368 Å.

The first step in inferring prominence mass is to determine how much coronal radiation is being absorbed as it passes through the prominence. The observational measure of extinction of coronal radiation, which for 171 Å, 195 Å, and 368 Å radiation arises only from hydrogen and helium continuum absorption and for 625 Å radiation arises from hydrogen continuum absorption, is represented by an extinction factor, α. If σ is the mean absorption cross section for radiation passing through a prominence, the extinction factor for radiation traveling in the direction $\hat{\mathbf{s}}$ over a distance ℓ is

$$\alpha = e^{-\int_0^\ell n\,\sigma\,ds}. \quad (1)$$

Here n is the total number density of all atoms and ions of H and He (note we assume He^{++} is negligible), and σ is given by

$$\sigma = f_{\rm H}(1 - x_{\rm H})\,\sigma_{\rm H} + f_{\rm He}(1 - x_{\rm He})\,\sigma_{\rm He} + f_{\rm He}\,x_{\rm He}\,\sigma_{\rm He^+}, \quad (2)$$

where the fractional hydrogen and helium abundances (by number) are represented by $f_{\rm H}$ and $f_{\rm He,}$ and the H and He ionization fractions by $x_{\rm H} = n_{\rm H^+}/(n_{\rm H} + n_{\rm H^+})$and $x_{\rm He} = n_{\rm He^+}/(n_{\rm He} + n_{\rm He^+})$. $\sigma_{\rm H}$, $\sigma_{\rm He}$, and $\sigma_{\rm He^+}$ are the photoionization cross sections (for the particular line of interest) for H, He, and He^+, respectively. We assume that the absorbing material is composed only of hydrogen and helium, so

$$f_{\rm H} + f_{\rm He} = 1. \quad (3)$$

If σ is uniform throughout the prominence, and if we define the column density by

$$N = \int_0^\ell n\,ds, \quad (4)$$

it follows that

$$\alpha = e^{-N\sigma} \quad (5)$$

$$-\ln\alpha = \mathrm{N}\sigma. \quad (6)$$

As described in Appendix A, applying this to a prominence visible in two spectral lines allows the determination of the helium abundance. By using 625 Å and 368 Å, we obtained He^0/H^0 abundance ratios in the range 0.23–0.51. These are much higher than those found by Del Zanna et al. (2004), which is likely due to the higher opacity ($\tau \gg 1$) of prominence material at longer EUV wavelengths which places upper limits on the measured H^0 column masses.

3.1. Opacity Issues

The approach described in Appendix A is negatively impacted by problems with saturation at longer EUV wavelengths that create large errors in the total mass calculations (Schmieder et al. 1999; Heinzel et al. 2008). Saturation is problematic because it means that the column density measured via the equation for photoionization only yields a lower bound, instead of an accurate definitive value. It results in a very small extinction factor, α, leading to uncertainties in the measurement technique that make the accurate determination of α impossible (Gilbert et al. 2005). Some theoretical models (Anzer & Heinzel 2005; Heinzel et al. 2008) have found the opacity in 625 Å to be much larger than in 195 Å (also note the much larger photoionization cross section for the longer wavelengths in Figure 1) that leads to an underestimation of the mass from 625 Å. A good illustration of the effect of different opacities in the present study is that prominences simultaneously visible in 625 Å and 195 Å yield measurements of drastically different masses (~3 times as large when using 195 Å). From our analysis, we find that the inferred total masses are systematically lowest in the Mg X (625 Å) line, followed by Mg IX (368 Å) (see Section 4). This is likely a consequence of the saturation problems discussed above. Filling factor effects also need to be considered in saturation issues. Many prominences demonstrate a fine structure, and if we are averaging over whole pixels where only part of the pixel area contains extremely high density (saturation), our average column density calculation will not change with increasing prominence density (beyond the saturation limit) and will thus lead to underestimations of the mass.

Because the saturation of the 625 Å and 368 Å lines has a potentially large impact on the total mass quantities, we used an alternative approach to obtain the two-dimensional (2D) mass "maps" of prominences in various EUV lines. We invoke the method of Gilbert et al. (2005, 2006) for each line separately, with the assumed composition of 90% hydrogen and 10% helium and the assumed ionization fractions $\chi_{\rm H} = 0.5$ and $\chi_{\rm He} = 0.1$ (see Gilbert et al. 2005 for a discussion on how varying these parameters affects the uncertainties in the density and mass calculations). These assumed values are based on estimates provided by non-LTE modeling efforts (Anzer & Heinzel 1999; Heinzel et al. 2008; and Labrosse & Gouttebroze 2004) and fall into the ranges used in the sensitivity study in Gilbert et al. (2005).

3.2. Constructing Mass Maps

The EUV observations were analyzed using an IDL routine that allows the user to select the pixels in each image containing prominence material, determine the limb radius, and estimate the depth of the prominence and the mean altitude of the material from the solar surface (Kilper 2009).

Since the mass calculation is highly sensitive to the values of the pixels chosen, especially when calculating the amount of foreground radiation (see below for more details on the error analysis), the steps that greatly impact those calculations are repeated 10 times to reduce statistical error. The scale height of the coronal emission is measured by finding the slope of a semi-log plot of the line emission versus the radius. To obtain the background radiation, we interpolate between points that are on either side of the prominence material. Since the amount of coronal radiation along a radial scan of the quiet Sun generally follows a symmetric logarithmic distribution that is peaked at the edge of the limb, we correct for small

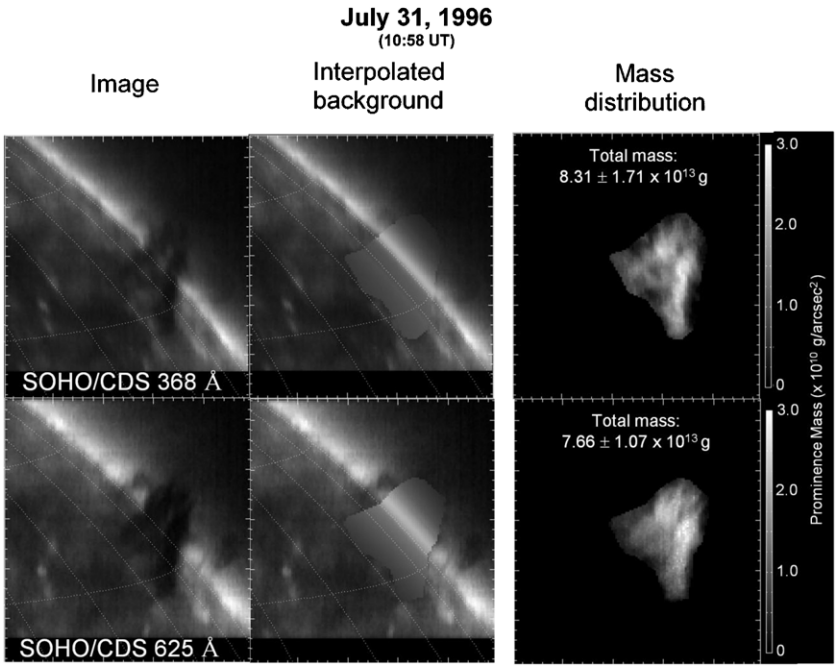

Figure 2. Example showing the original images in CDS Mg IX and Mg X containing the prominence, the interpolated background image, and the resulting mass maps.

deviations in coronal emission by using a power law to smooth over any anomalies and provide a much better estimate of the coronal radiation around the prominence material. The code automatically interpolates the amount of coronal emission at all data pixels of the prominence between the two corrected radial scans, providing a map of the interpolated background radiation and effectively "deleting" the prominence material.

Using the interpolated image together with the real image, and accounting for the amount of radiation originating in front of the prominence (foreground radiation $= I_f$), we are able to obtain an extinction factor for each pixel, and thus infer a mass per pixel. The resulting "maps" showing the distribution of mass in the different lines allow a comparison of the relative spatial distribution of neutral helium and hydrogen.

3.3. EUV Absorption Error Analysis

Sources of error (other than the opacity issues discussed above) include those inherent in the method (a detailed description of the assumptions involved can be found in Gilbert et al. 2005). The determination of α introduces error because it involves looking at intensity measurements in a small region on the disk and just off the limb. The space between the intensity measurements on the disk and just off the limb needs to be small ($\sim$6 pixels apart) and displays relatively uniform properties throughout the localized region, so to mitigate the error associated with individual pixel fluctuations, we repeated the calculation 10 times for each measurement using several pairs of data pixels to estimate the foreground radiation. We also performed various interpolations of the background radiation at different locations to study the variation. Trial runs showed that 10 repetitions were enough to reduce this source of error by 2–3 times, but a greater number of repetitions did not continue decreasing the spread in the calculated masses.

Error was also reduced by prudent data selection; we excluded prominences near active regions and coronal holes to assure a better determination of the coronal radiation around each prominence. Instrumental effects were tested by several comparisons, and all were found to be relatively insignificant. For example, analyses of simultaneous *TRACE* and EIT observations (at either 171 Å or 195 Å) measured similar mass values, despite different resolution, exposure times, instrumentation, etc. There were also no changes detected between different exposure times and pixel sizes for EIT 195 Å observations, comparable prominence observations before and after loss of communication with *SOHO* in 1998 June, and the different observing programs used for the CDS observations.

Due to the limitations associated with saturation issues in the Mg X (and possibly Mg IX) line, the results focus on the spatial mass distributions measured via the different coronal lines. We present a summary of the total calculated masses for completeness, but emphasize that the mass values for the 625 Å and 368 Å observations should be considered as the lower bounds of the total prominence masses, and not definitive values. It should also be noted that relatively hot prominence plasma emitting in the 171 Å band (which has a broad temperature response with a peak near 1 MK) may be present in some cases, and this will affect the mass measurements.

4. RESULTS

As an illustrative example of the method described above, Figure 2 shows the CDS intensity images, the interpolated background images, and the mass per pixel "map" for the 1996 July 31 prominence. The images and mass maps for the other eight prominences studied are shown in Appendix B. Note that the interpolated background image for the prominence in Figure 2 is much more accurate for the portion of the prominence visible above the solar limb relative to the portion visible against the solar disk because there is very little background coronal emission to be absorbed when the prominence is located on the disk. This is also the case for prominences studied on 1997 May 9, 1999 March 20, 1999 March 23, 1999 October 12, and 2005 May 18.

Measurements and error values of the total prominence masses are displayed in Table 2; the errors account for those

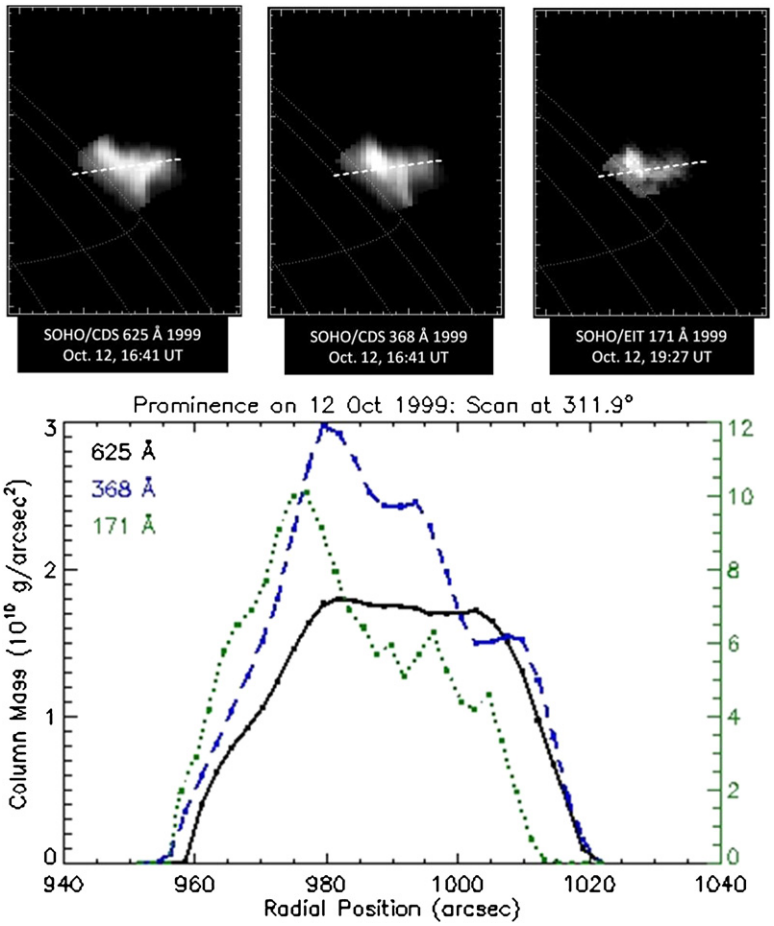

Figure 3. 1999 October 12 scans in 625 Å (top left, solid line in plot), 368 Å (top middle, dashed line in plot), and 171 Å (top right, dotted line in plot) mass maps plotted to demonstrate qualitative spatial differences in mass concentrations in the three lines in a prominence located at position angle 310°. Note the differences in the scale in the 171 Å plot (right) with respect to the others. This is because the measured masses are significantly larger in 171 Å (see the discussion above).

(A color version of this figure is available in the online journal.)

involved with the analytical method and the data (see Section 3.2), but exclude any error resulting from the high opacity and saturation of the lines.

Figure 3 shows scans of the mass maps and resulting plots from the 625 Å, 368 Å, and 171 Å observations for the prominence on 1999 October 12. The plots of the 368 Å and 171 Å scans are similar in shape while the 625 Å scan shows a flattened, extended plateau. This prominence is the clearest and most dramatic example that saturation in 625 Å can lead to an underestimation of mass in the deepest part of the prominence, consistent with the discussion in Section 3.1.

Because of the limited availability of prominence observations suitable for this study, eight of the nine prominences were imaged at only one or two times. However, over 25 individual observations of the prominence on 2005 May 18 are available, allowing some measure of the evolution of mass distribution over the course of the day. This prominence exhibits apparent flows along field lines throughout the day and the spatial distribution of the continuum absorption (and thus the mass) is qualitatively similar for 625 Å and 171 Å, and 195 Å (Figure 4), despite the differing opacities at those wavelengths.

5. DISCUSSION

The total prominence mass calculations in Table 2 show a consistently lower mass in the 625 Å observations compared to the other lines. The significant difference in total mass between the 625 Å and 195 Å lines indicates that the much higher opacity at 625 Å may be causing a saturation of the continuum absorption (as suggested in Heinzel et al. 2008), and thus a potentially large underestimation of mass (see Figure 3). While the opacity at 368 Å has not yet been modeled, it also has a large photoionization cross section compared to 195 Å, and the significant difference between the masses calculated from those lines suggests that the opacity of prominences is also large at 368 Å, indicating that saturation may also be an issue for this line. At 171 Å, the photoionization cross section is even smaller than at 195 Å, which should mean that the opacity is low, yet the masses measured from the 171 Å observations are almost always smaller than those from 195 Å. The likely explanation is that hot prominence plasma is emitting in 171 Å (peaking at 1.0 MK) and reducing the amount of continuum absorption that is measured, leading to a lower mass estimate (previously found by Kucera et al. 1998 and Engvold et al. 2001). Quantitatively, the mass estimates from 195 Å (at 1.5 MK) benefit from a good combination of low opacity and negligible internal emission to provide the most accurate values of the total mass. Masses obtained in the present work are consistent with those found in our previous work (Gilbert et al. 2005, 2006). Gilbert et al. (2006) used 195 Å data to obtain masses for 10 quiescent prominences, finding an average mass of 4.18×10^{14} g. The average mass derived from 195 Å in the present

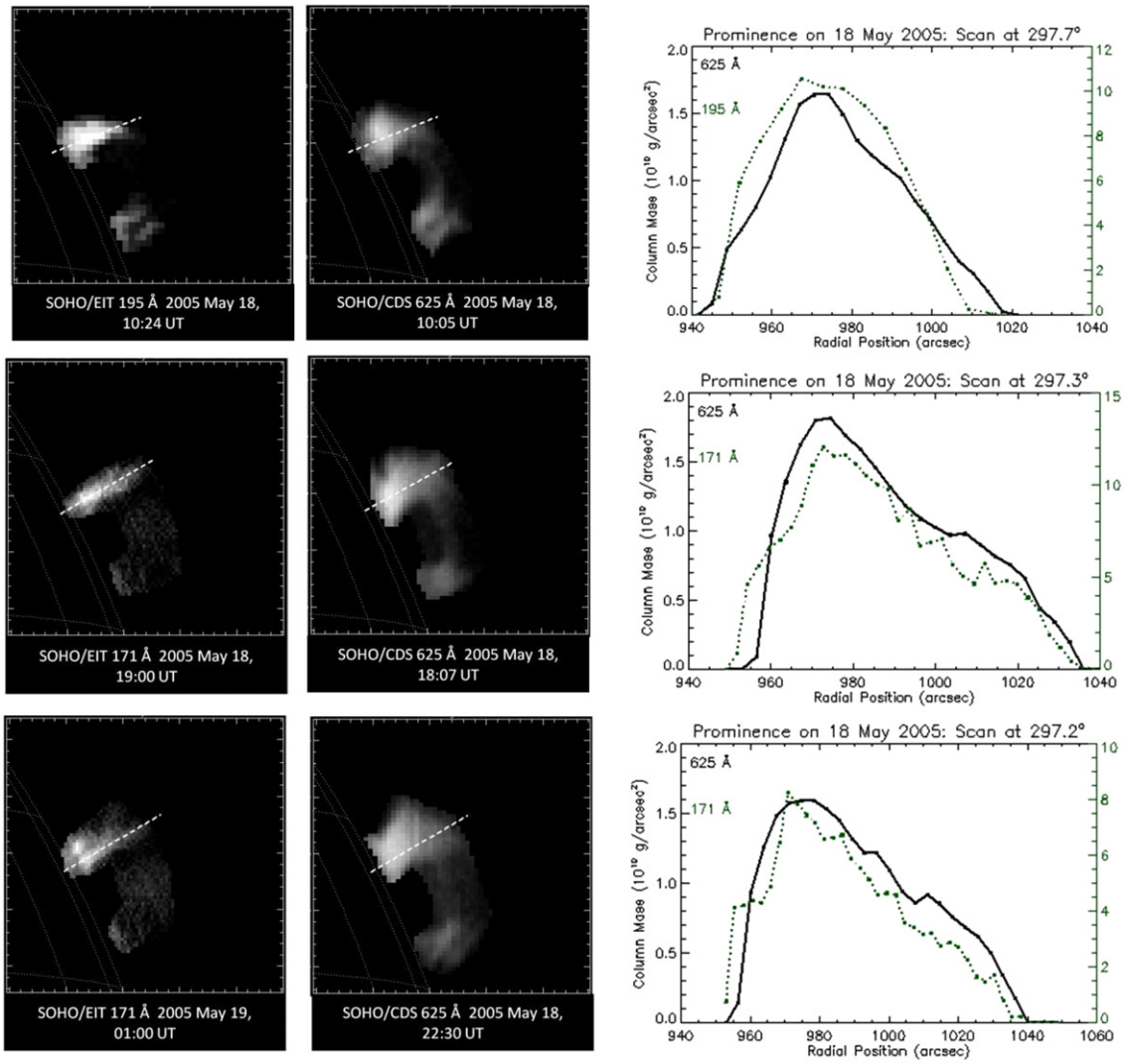

Figure 4. 2005 May 18 scans in mass maps plotted to demonstrate spatial differences in mass concentrations in two lines in a prominence located at position angle 297°: 195 Å (top left) and 625 Å (top center), 171 Å (middle left) and 625 Å (middle center), and 171 Å (bottom left) and 625 Å (bottom center). The plots in the right column show the relative distributions, where 625 Å is shown as the solid lines and 195 Å and 171 Å are shown as dotted lines. Note the differences in the scale in the 171 Å and 195 Å plots with respect to 625 Å. This is because the measured masses are significantly larger in 171 Å and 195 Å than 625 Å (see the discussion above). (A color version of this figure is available in the online journal.)

Table 2
Total Prominence Masses

Date	Mass (10^{13} g) in Mg X (625 Å)	Mass (10^{13} g) in Mg IX (368 Å)	Mass (10^{13} g) in Fe XII (195 Å)	Mass (10^{13} g) in Fe IX (171 Å)
1996 Jul 31	8.25 ± 1.28	8.31 ± 1.71	21.41 ± 1.96	15.50 ± 2.48
1997 May 9	4.65 ± 0.62	5.99 ± 1.27	13.06 ± 2.21	7.13 ± 2.03[a]
1997 May 14	1.04 ± 0.06	1.32 ± 0.21	...	...
1997 Aug 7	1.29 ± 0.37	1.78 ± 0.60	...	...
1999 Mar 20	3.54 ± 0.54	4.16 ± 0.68	11.04 ± 2.81	7.29 ± 2.56[a]
1999 Mar 23	3.35 ± 0.89	4.72 ± 1.21	7.79 ± 1.41	...
1999 Jun 2	2.96 ± 0.77	...	10.56 ± 2.49	8.02 ± 2.30
1999 Oct 12	2.86 ± 0.57	3.90 ± 1.01	10.85 ± 4.35	8.73 ± 3.08
2005 May 18[b]	4.83 ± 1.74	...	13.07 ± 3.52	14.16 ± 4.21

Notes.
[a] Averaged over two mass maps.
[b] Averaged over eighteen 625 Å, three 171 Å, and twelve 195 Å mass maps.

work is 1.25×10^{14} g, while that derived from 171 Å is 1.01×10^{14} g. The average mass derived in both 625 Å and 368 Å is 0.43×10^{14} g. The finding that saturation in absorption is occurring for the longer (relative to 171 Å and 195 Å) wavelength lines and that this saturation limits the ability to obtain accurate relative abundances is a significant result that will impact future studies of prominence mass using EUV absorption.

Parameters such as the helium abundance and the hydrogen and helium ionization fractions are critical to accurate models of the prominence plasma, and observationally determining

them would advance our overall knowledge of the fundamental physics of prominences. In theory, prominence plasma that is thin enough could be unaffected by saturation, despite the high opacity, and an accurate helium abundance could be measured with our method. Obtaining a strong enough signal-to-noise ratio in such a thin plasma would require more sensitive instruments than are currently available, but a successor to the CDS instrument, with data available in all the relevant spectral regimes, on a future space-based observatory could make this possible. Alternatively, spectral models of these EUV lines could become sufficiently advanced such that the saturated continuum absorption values could be used to derive the actual column densities. In reality, a combination of these solutions is likely required to obtain the observational parameters that the prominence modelers require.

We thank Joe Gurman for sharing his knowledge of the EIT observations and his help in revising the manuscript, and Petr Heinzel and Nicolas Labrosse for their insightful comments and help with understanding the saturation issues. We also thank Tom Holzer for helping make sure the derivation in Appendix A is correct. This work was partially supported by NASA grant NNX07AI10G. *SOHO* is a mission of international cooperation between ESA and NASA.

APPENDIX A

DERIVING PROMINENCE MASS AND HELIUM ABUNDANCE

Recalling Equations (1)–(6) in Section 3,

$$\alpha = e^{-\int_0^\ell n\,\sigma\,ds} \tag{A1}$$

$$\sigma = f_{\rm H}(1-x_{\rm H})\sigma_{\rm H} + f_{\rm He}(1-x_{\rm He})\sigma_{\rm He} + f_{\rm He}\,x_{\rm He}\,\sigma_{\rm He^+} \tag{A2}$$

$$f_{\rm H} + f_{\rm He} = 1 \tag{A3}$$

$$N = \int_0^\ell n\,ds \tag{A4}$$

$$\alpha = e^{-N\sigma}. \tag{A5}$$

For convenience, we define

$$\varepsilon = -\ln\,\alpha = N\sigma \tag{A6}$$

we can utilize Equations (A2) and (A6) to write ε in the form

$$\varepsilon = \varepsilon_{\rm H} + \varepsilon_{\rm He} + \varepsilon_{\rm He^+}, \tag{A7}$$

where

$$\varepsilon_{\rm H} = Nf_{\rm H}(1-x_{\rm H})\sigma_{\rm H} \tag{A8}$$

$$\varepsilon_{\rm He} = Nf_{\rm He}(1-x_{\rm He})\sigma_{\rm He} \tag{A9}$$

$$\varepsilon_{\rm He^+} = Nf_{\rm He}\,x_{\rm He}\,\sigma_{\rm He}. \tag{A10}$$

Note that although we define the quantities $\varepsilon_{\rm H}$, $\varepsilon_{\rm He}$, and $\varepsilon_{\rm He^+}$, the only observed quantity is ε, so the parameters we wish to determine (such as N and $f_{\rm He}$) are expressed in terms of ε (not in terms of $\varepsilon_{\rm H}$, $\varepsilon_{\rm He}$, and $\varepsilon_{\rm He^+}$). Since we are assuming that absorption occurs only through ionization, there is a simplification for Equations (A7)–(A10) at two of our wavelengths of interest (namely, 625 Å and 368 Å):

$$\varepsilon_{\rm He\,625} = \varepsilon_{\rm He^+\,625} = \varepsilon_{\rm He^+\,368} = 0. \tag{A11}$$

Making use of Equations (A7)–(A11), we can write expressions for ε at three wavelengths of interest:

$$\varepsilon_{625} = \varepsilon_{\rm H\,625} = Nf_{\rm H}(1-x_{\rm H})\sigma_{\rm H\,625} \tag{A12}$$

$$\varepsilon_{368} = \varepsilon_{\rm H\,368} + \varepsilon_{\rm He\,368} = Nf_{\rm H}(1-x_{\rm H})\sigma_{\rm H\,368} + Nf_{\rm He}(1-x_{\rm He})\sigma_{\rm He\,368} \tag{A13}$$

$$\varepsilon_{195} = \varepsilon_{\rm H\,195} + \varepsilon_{\rm He\,195} + \varepsilon_{\rm He^+\,195} = Nf_{\rm H}(1-x_{\rm H})\sigma_{\rm H\,195} + Nf_{\rm He}(1-x_{\rm He})\sigma_{\rm He\,195} + Nf_{\rm He}\,x_{\rm He}\,\sigma_{\rm He^+\,195} \tag{A14}$$

A.1. Determining Mass and Helium Abundance from Observations at 625 Å and 368 Å

We can now obtain expressions for N, $f_{\rm H}$, and $f_{\rm He}$ for various observational cases. Let us first consider the case where we have observationally determined ε_{625} and ε_{368}. Rearranging Equation (A12), we can write

$$Nf_{\rm H}(1-x_{\rm H}) = \varepsilon_{625}/\sigma_{\rm H\,625}. \tag{A15}$$

Making use of Equation (A15), we can rewrite Equation (A13) in the form

$$Nf_{\rm He}(1-x_{\rm He}) = \left(\varepsilon_{368} - \varepsilon_{625}\,\frac{\sigma_{\rm H\,368}}{\sigma_{\rm H\,625}}\right)\Big/\sigma_{\rm He\,368}. \tag{A16}$$

It is useful to rearrange Equations (A15) and (A16) in the following way:

$$Nf_{\rm H} = \frac{\varepsilon_{625}}{\sigma_{\rm H\,625}(1-x_{\rm H})} \tag{A17}$$

$$Nf_{\rm He} = \frac{\varepsilon_{368} - \varepsilon_{625}\,\frac{\sigma_{\rm H\,368}}{\sigma_{\rm H\,625}}}{\sigma_{\rm He\,368}(1-x_{\rm He})}. \tag{A18}$$

Making use of Equation (A3), we can now add Equations (A17) and (A18) to obtain an expression for the column density, N:

$$N = \frac{\varepsilon_{368}}{\sigma_{\rm He\,368}}\,\frac{1}{(1-x_{\rm He})} + \frac{\varepsilon_{625}}{\sigma_{\rm H\,625}} \times\left[\frac{1}{(1-x_{\rm H})} - \frac{\sigma_{\rm H\,368}}{\sigma_{\rm He\,368}}\,\frac{1}{(1-x_{\rm He})}\right]. \tag{A19}$$

Dividing Equation (A18) by Equation (A17), we obtain

$$\frac{f_{\rm He}}{f_{\rm H}} = \left(\frac{\varepsilon_{368}}{\varepsilon_{625}} - \frac{\sigma_{\rm H\,368}}{\sigma_{\rm H\,625}}\right)\frac{\sigma_{\rm H\,625}}{\sigma_{\rm He\,368}}\,\frac{(1-x_{\rm H})}{(1-x_{\rm He})}. \tag{A20}$$

Referring back to Equation (3), it is readily shown that

$$f_{\rm H} = \frac{1}{1 + f_{\rm He}/f_{\rm H}} \tag{A21}$$

$$f_{\rm He} = 1 - f_{\rm H}. \tag{A22}$$

Finally, we can write the column mass, M, in the form

$$M = N\,m_{\rm H}(f_{\rm H} + 4\,f_{\rm He}). \tag{A23}$$

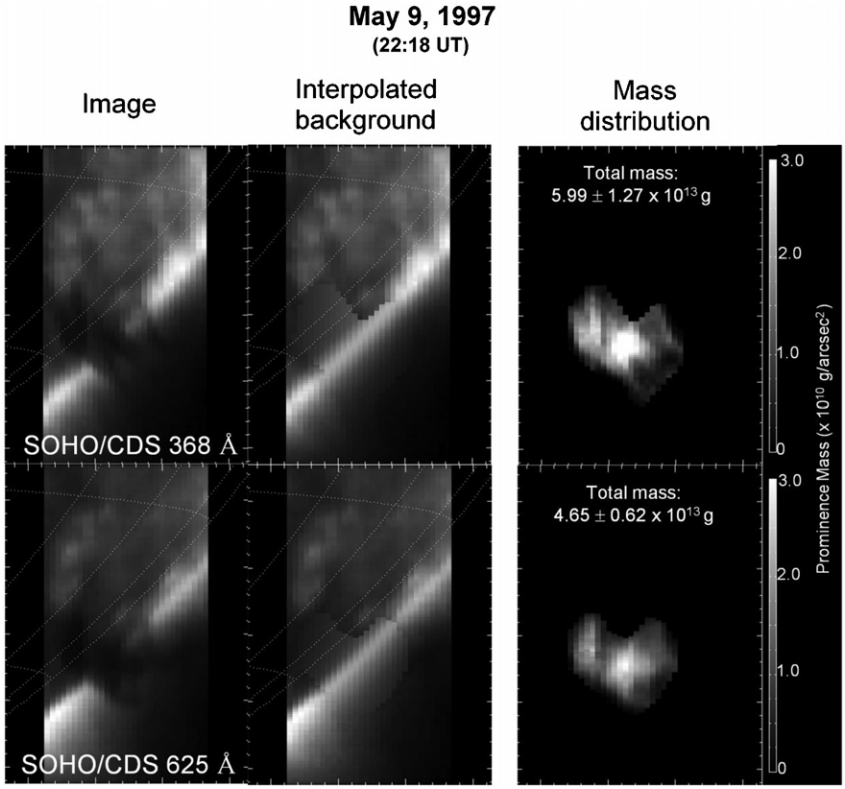

Figure 5. Images, interpolated backgrounds, and mass maps, for 1997 May 9.

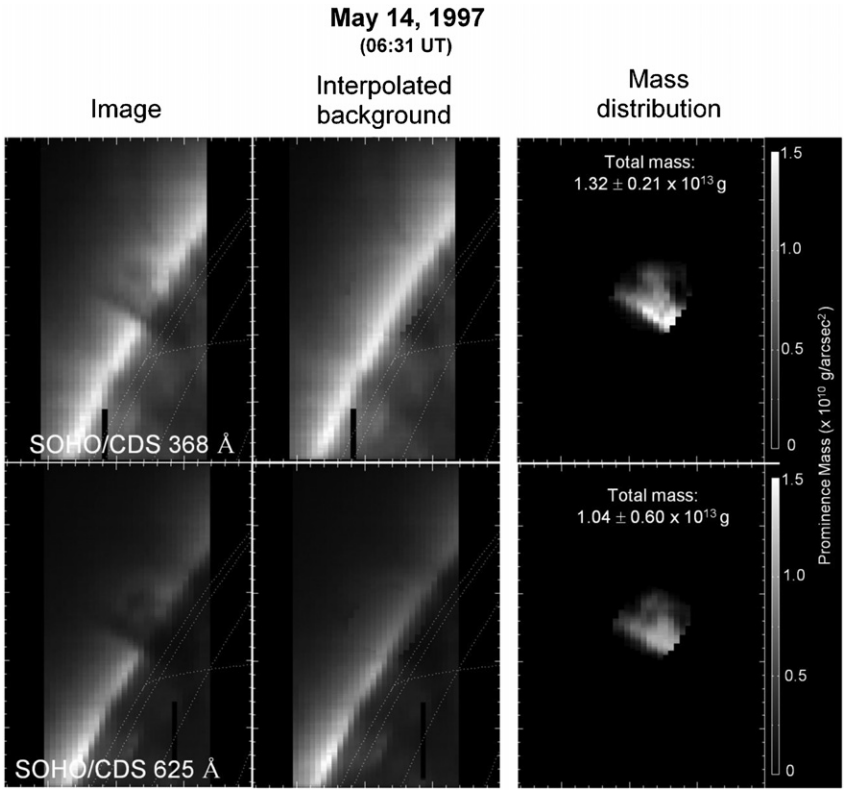

Figure 6. Images, interpolated backgrounds, and mass maps, for 1997 May 14.

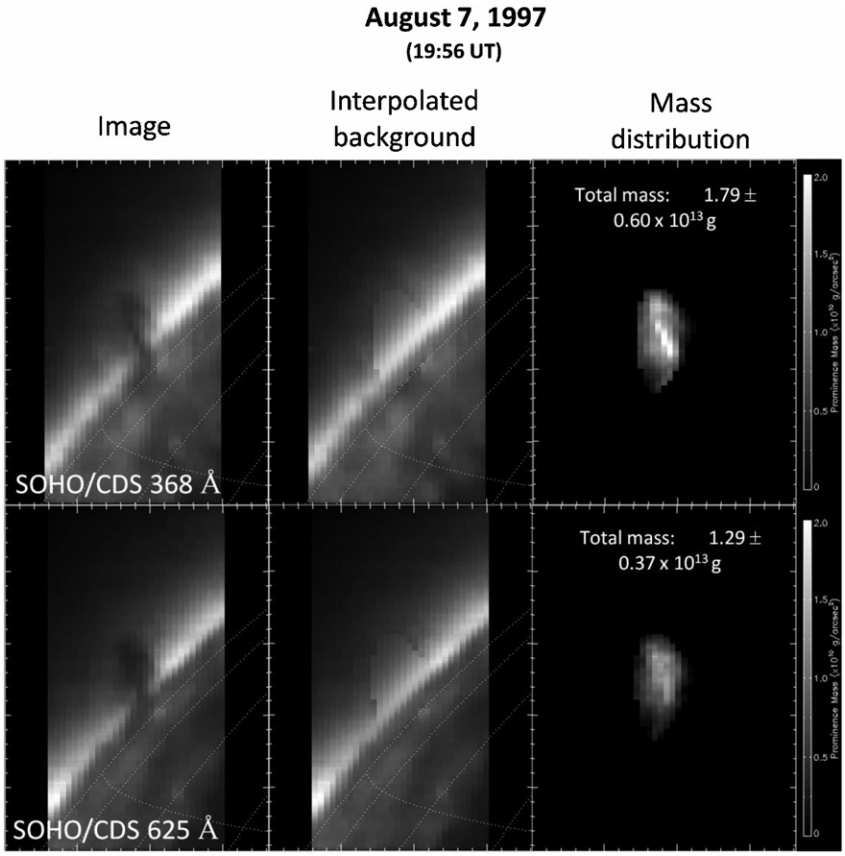

Figure 7. Images, interpolated backgrounds, and mass maps, for 1997 August 7.

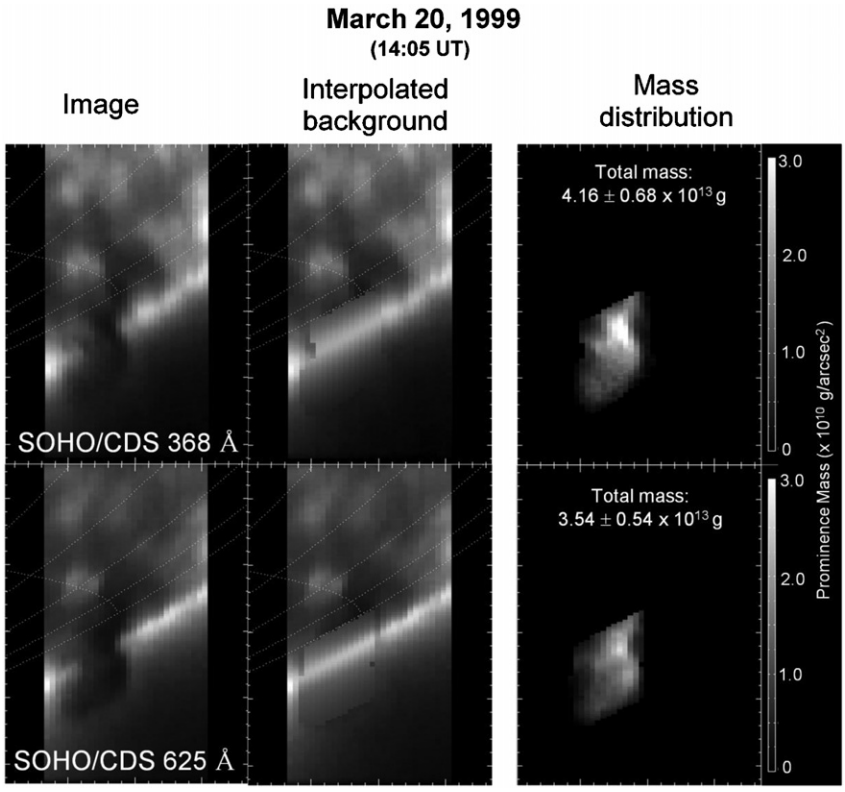

Figure 8. Images, interpolated backgrounds, and mass maps, for 1999 March 20.

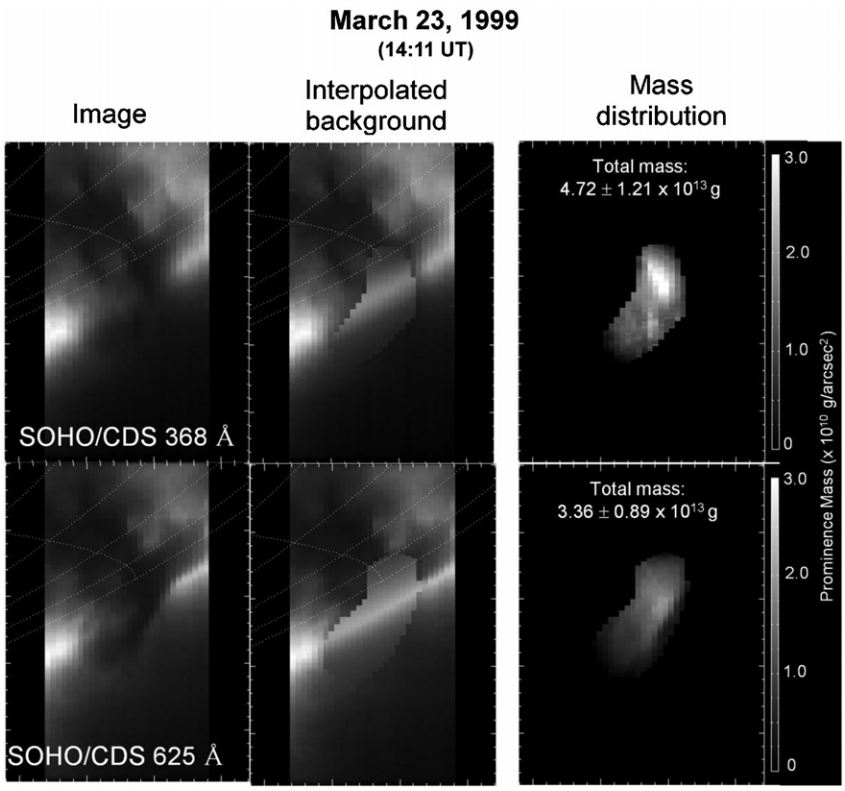

Figure 9. Images, interpolated backgrounds, and mass maps, for 1999 March 23.

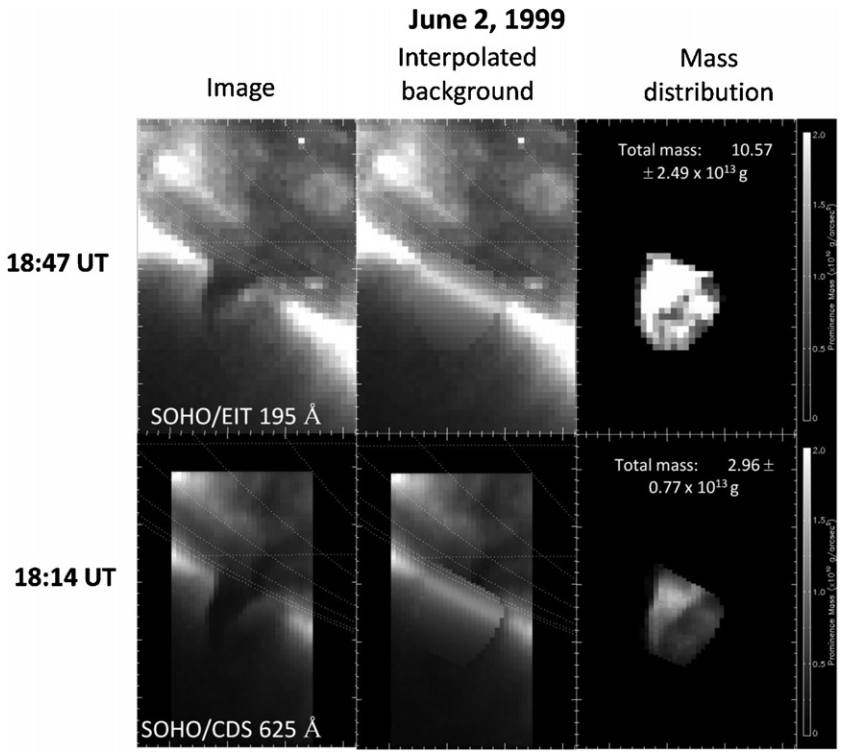

Figure 10. Images, interpolated backgrounds, and mass maps, for 1999 June 2.

Looking back at Equations (A19)–(A23), we see that it has been possible to write the column density, the column mass, and the hydrogen and helium fractions (by number) in terms of the two observed quantities ε_{625} and ε_{368}, the three known cross sections $\sigma_{\mathrm{H}\,625}$, $\sigma_{\mathrm{H}\,368}$, and $\sigma_{\mathrm{He}\,368}$, and the two unknown ionization fractions x_{H} and x_{He}. The total prominence mass can

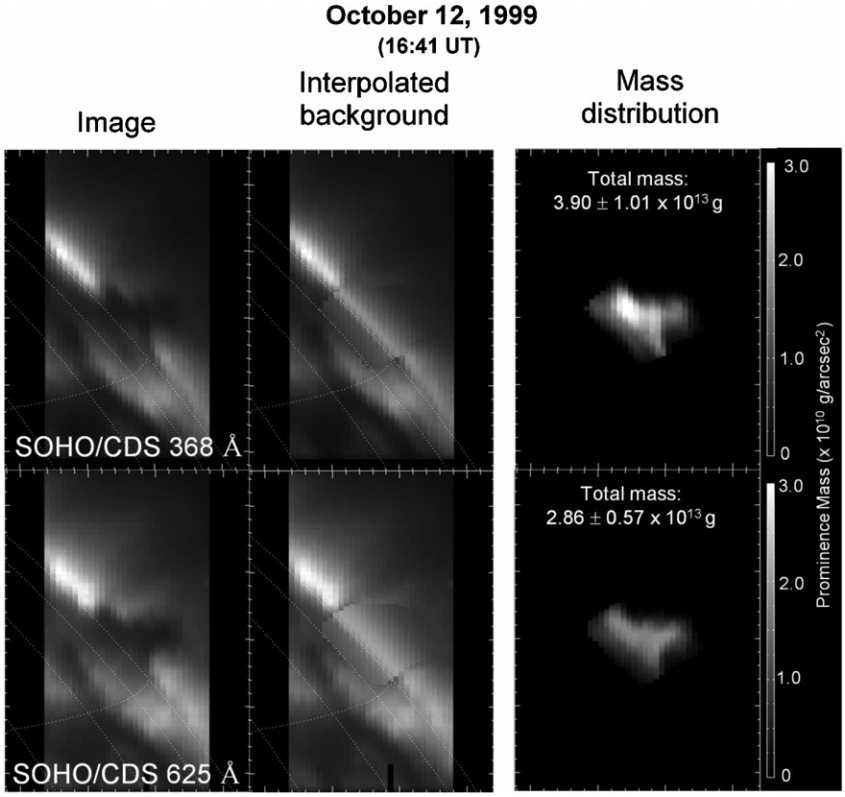

Figure 11. Images, interpolated backgrounds, and mass maps, for 1999 October 12.

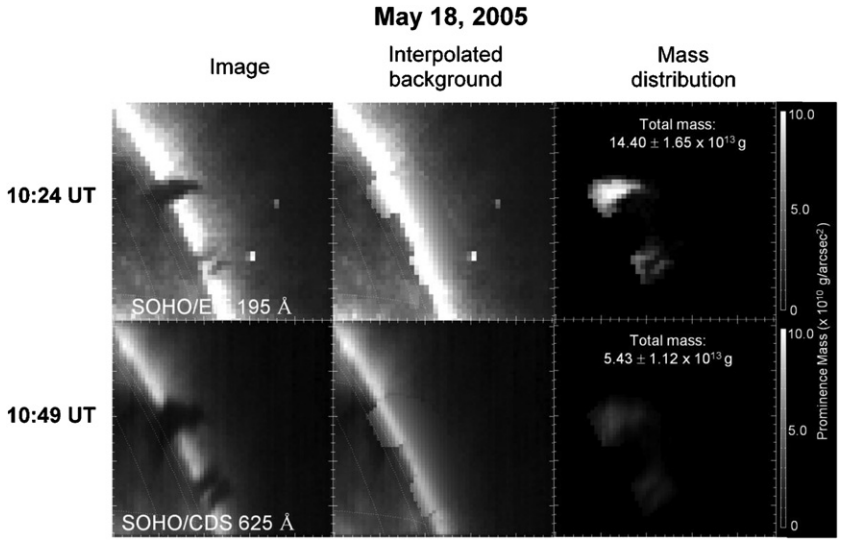

Figure 12. Images, interpolated backgrounds, and mass maps, for 2005 May 18.

now be determined by summing all values of M (times a pixel area) over the whole prominence if a measurement is made for each pixel.

APPENDIX B

MASS DISTRIBUTION OF THE REMAINING EIGHT PROMINENCES

Figures 5–12 show the mass distribution for each case.

REFERENCES

Anzer, U., & Heinzel, P. 1999, A&A, 349, 974
Anzer, U., & Heinzel, P. 2005, ApJ, 622, 714
Delaboudinière, J.-P., et al. 1995, Sol. Phys., 162, 291
Del Zanna, G., Chiuderi Drago, F., & Parenti, S. 2004, A&A, 420, 307
Engvold, O., Jakobsson, H., Tandberg-Hanssen, E., Gurman, J. B., & Moses, D. 2001, Sol. Phys., 202, 293
Gilbert, H. R., Falco, L. E., Holzer, T. E., & MacQueen, R. M. 2006, ApJ, 641, 606
Gilbert, H. R., Holzer, T. E., & MacQueen, R. M. 2005, ApJ, 618, 524
Golub, L., et al. 1999, Phys. Plasmas, 6, 2205
Handy, B. N., et al. 1999, Sol. Phys., 187, 229
Harrison, R. A., et al. 1995, Sol. Phys., 162, 233
Heinzel, P., Anzer, U., & Schmieder, B. 2003, Sol. Phys., 216, 159
Heinzel, P., Schmieder, B., & Tziotziou, K. 2001, ApJ, 561, L223
Heinzel, P., et al. 2008, ApJ, 686, 1383

Keady, J. J., & Kilcrease, D. P. 2000, in Allen's Astrophysical Quantities, ed. A. N. Cox (New York: AIP), 106
Kilper, G. 2009, PhD thesis, Rice Univ.
Kucera, T. A., Andretta, V., & Poland, A. I. 1998, Sol. Phys., 183, 107
Labrosse, N., & Gouttebroze, P. 2004, ApJ, 617, 614
Mein, N., Schmeider, B., Deluca, E. E., Heinzel, P., Mein, P., Malherbe, J.-M., & Staiger, J. 2001, ApJ, 556, 438
Penn, M. 2000, Sol. Phys., 197, 313
Schmieder, B., Heinzel, P., Kucera, T., & Vial, J. C. 1998, Sol. Phys., 181, 309
Schmieder, B., Kotrč, P., Heinzel, P., Kucera, T., & Andretta, V. 1999, in Magnetic Fields and Solar Processes, ed. A. Wilson (ESA SP-448; Noordwijk: ESA), 439
Schmieder, B., Mein, N., Deng, Y., Dumitrache, C., Malherbe, J.-M., Staiger, J., & Deluca, E. E. 2004, Sol. Phys., 223, 119
Schmieder, B., Tziotziou, K., & Heinzel, P. 2003, A&A, 401, 361